Using a quantum well heterostructure to study the longitudinal and transverse electric field components of a strongly focused laser beam

G. Kihara Rurimo,[a] M. Schardt, S. Quabis,[b] S. Malzer, Ch. Dotzler, A. Winkler, G. Leuchs, and G. H. Döhler
Max-Planck-Research-Group, Institute of Optics, Information and Photonics, Günther Scharowsky-Strasse 1/Bau 24, University of Erlangen, D-91058 Erlangen, Germany

D. Driscoll, M. Hanson, and A. C. Gossard
Materials Department, University of California, Santa Barbara, California 93116

S. F. Pereira
Faculty of Applied Sciences, Optics Research Group, Delft University of Technology, Lorentzweg 1, 2628 CJ Delft, Netherlands

(Received 20 December 2005; accepted 19 April 2006; published online 25 July 2006)

We report a method to measure the electric energy density of longitudinal and transverse electric field components of strongly focused polarized laser beams. We used a quantum well photodetector and exploited the polarization dependent optical transitions of light holes and heavy holes to probe the electric field distribution in the focal region. A comparison of the measured photocurrent spectra for radially and azimuthally polarized beams at the light and heavy hole absorption peaks provides a measure of the amount of the longitudinal electric field component. © *2006 American Institute of Physics*. [DOI: 10.1063/1.2214207]

I. INTRODUCTION

It is well known that in the regime of strong focusing a vectorial theory[1] is required to describe the electric field distribution in the focal region. Due to polarization effects in the focus of a linearly polarized input beam, there exists a transverse electric field component orthogonally polarized to the input beam and a longitudinal electric field component parallel to the direction of beam propagation.[2] Approximately 20% of the electric energy density is contained in the longitudinal field when a linearly polarized beam is focused using a microscope objective of numerical aperture (NA =0.9).

The longitudinal electric field component is of great interest for many applications.[3–5] For a radially polarized beam, which is rotationally symmetric also in its polarization properties, 50% of the electric energy is confined in the longitudinal component. This can be enhanced to more than 80% by using an annular aperture. In contrast, an azimuthally polarized beam is the best choice when a purely transverse field is required at the focal region.[6]

Several experimental studies of the focal region have been reported. These can be divided into two categories, namely, the detection of the focal intensity[7] distribution and the probing of the focal electric field distribution. An overview of the various experimental realizations of these detection schemes in both categories is given in the next paragraphs.

To measure the focal intensity distribution of a weakly focused beam, a charge coupled device (CCD) camera has been used.[8] The experimental result was in excellent agreement with the prediction from theory. In this case, however, polarization effects are too small to be detected. In the regime of strong focusing, a knife edge method[2,9] can be used to measure the intensity distribution in the focal region. In this case, polarization effects can be seen if the detection angle is sufficiently large. As an alternative to provide for the necessary high numerical aperture detection, a scanning near field optical microscope (SNOM) fiber tip[10] can also be used. In principle, it is even possible to measure phase and amplitude with a SNOM,[11] however, the sensitivity for longitudinal and transverse components can differ[12] and this discrepancy needs to be taken into account for the interpretation of the results.

Besides the experiments described above for the focal intensity measurements, several polarization sensitive measurements to detect the focal electric field distribution have been reported. The transverse electric field components E_x and E_y can be distinguished by using a polarizer[13] at the focal region, but the E_z component remains undetected. In contrast, if a tip is used to probe the focal region, the longitudinal field E_z can be detected with high lateral resolution. However, the detected signal is strongly influenced by the tip-field interaction and also depends on the dielectric constant of the tip material.[14–16] Another option to measure both the intensity or electric field distribution is to scan small metallic beads through the focus and detect the scattered light. Due to the fact that a dipole moment is induced by the external field, the emission characteristics of the bead depends on its position within the focus.[17] Instead of isotropic beads which do not have a defined axis, one can also use individual molecules oriented in three different mutually orthogonal directions to scan the electric energy distribution of

[a]Electronic mail: rurimo@kerr.physik.uni-erlangen.de
[b]Electronic mail: quabis@physik.uni-erlangen.de

all the three polarization directions separately.[18,19] A quantitative comparison is hindered by the fact that different detectors (molecules) have to be used for each of the polarization directions.

In this paper, we present a method to separately determine the amount of the electric field energy densities of the longitudinal and transverse electric field components using a semiconductor nanostructure. Semiconductor nanostructures are particularly suitable as polarization detectors. Excitonic absorption involving heavy holes is caused by in-plane polarized light only, whereas the major component of the dipole moment for light hole exciton absorption corresponds to a polarization perpendicular to the surface.[20,21] As the energies for heavy and light hole excitons differ significantly, one can easily distinguish between heavy and light hole absorptions. Moreover, the absorption can be detected conveniently by measuring the photocurrent, if the nanostructures are embedded in a pin diode. In this case the photogenerated electrons and holes contribute almost fully to the photocurrent as they are separated by the electric field present in the intrinsic region of the diode before they can recombine. The ideal nanostructure would be a self-assembled quantum dot.[22] In this case, spatially resolved photocurrent measurements would allow for the determination of the actual distribution of in-plane and longitudinal electric field components in the focal region of strongly focused light beams. Such experiments are, however, rather demanding, as a single quantum dot is only weakly coupling to the light field. In the present work we have chosen a suitably designed quantum well nanostructure. Due to translational invariance of quantum wells, the photocurrents for the two polarizations reflect spatial averages over the whole focal region. However, significant information about the polarization can be deduced from the experiment by analyzing the data with the corresponding semiconductor model.

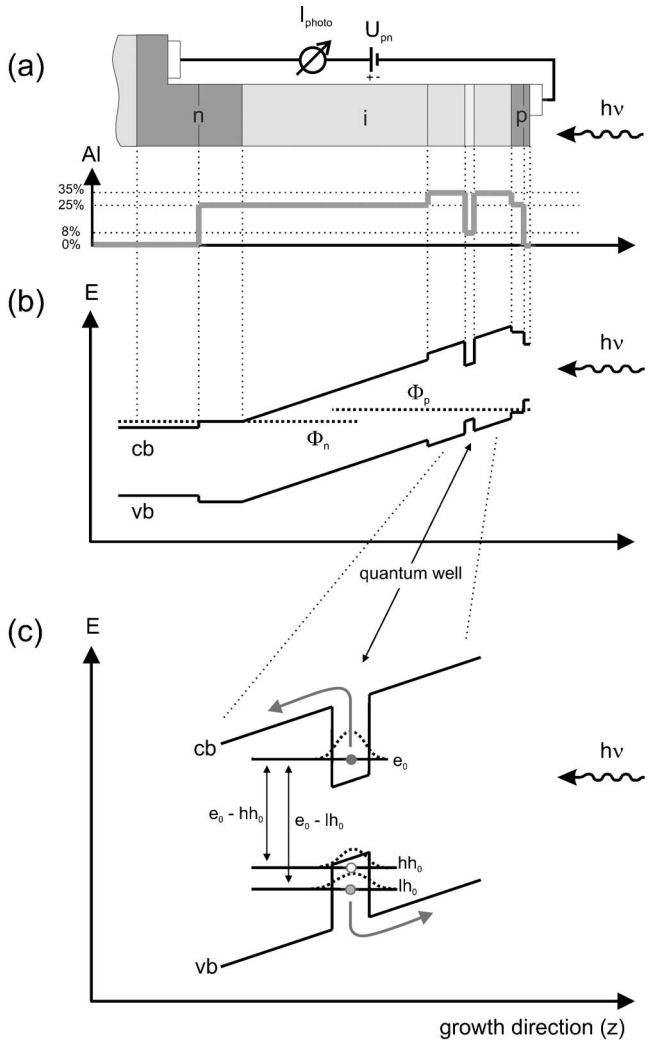

FIG. 1. (a) Schematic diagram of the sample layer structure with Al profile. The quantum well, 80 nm beneath the sample surface, is embedded in the *i* region of a pin diode. To allow for resonant interband excitation inside the quantum well only, the sample is made of $Al_xGa_{1-x}As$ with a sufficient Al content x to ensure optical transparency. (b) Band diagram (schematic) for a small reverse bias applied (for photocurrent measurements). (c) Close-up of the quantum well region denoting the electron, heavy, and light hole ground states. Photogenerated carriers can escape the barrier layers by thermal activation and contribute to the photocurrent.

II. DESIGN AND CHARACTERIZATION OF THE QUANTUM WELL STRUCTURE

The quantum well sample was grown by molecular beam epitaxy (MBE) on a semi-insulating GaAs substrate. Processing of individual devices was done by photolithography and wet-chemical etching. In Fig. 1, a schematic diagram of the sample design used for normal incidence illumination is presented.

The quantum well [see Fig. 1(c)] is embedded in the intrinsic region of a pin diode to enable photocurrent measurements by resonant interband excitation of carriers inside the quantum well [Fig. 1(b)]. To ensure optical transparency of the sample within our range of available wavelengths, the structure is composed of $Al_xGa_{1-x}As$ layers with sufficiently high aluminum content x. To enhance carrier localization the quantum well is embedded between two 50 nm wide barrier layers of intrinsic $Al_{0.35}Ga_{0.65}As$.

The quantum well is located 80 nm below the sample surface and consists of 25 monolayers ($\approx$7.1 nm) of undoped $Al_{0.08}Ga_{0.92}As$. These values were chosen by simulation to give the maximum splitting between light hole (lh) and heavy hole (hh) transitions. The splitting of the lh and the hh valence bands due to carrier confinement is dominated by the quantum well width, whereas the absolute transition energies for $e-\mathrm{lh}$ and $e-\mathrm{hh}$ interband transitions mainly scale with the bandgap inside the quantum well and thus with the aluminum concentration. For the range of wavelengths defined by the tuning range of our laser, we found 25 monolayers with 8% aluminum content to work best. The excitonic transition energy for the $e_0-\mathrm{hh}_0$ transition was calculated to be 1.582 eV (783.6 nm) and the $e_0-\mathrm{lh}_0$ transition as 1.602 eV (773.8 nm). These energies are well within the tuning range of our laser. The splitting between the two interband transitions is large enough to be easily resolved as individual peaks in the photocurrent spectrum. The photogenerated carriers are thermally activated over the barrier layers and separated by the electric field in growth direction, thus giving rise to a photocurrent.

It is well known[20,21] that the relative strength of the e_0

TABLE I. Polarization dependent transition probabilities at $k=0$ (first Brillouin zone) for interband dipole transitions in GaAs.

TE (purely transverse)	hh: 3/12 lh: 1/12
TM (purely longitudinal)	hh: 0 lh: 4/12

$-\mathrm{lh}_0$ and $e_0-\mathrm{hh}_0$ transitions is dependent on the polarization of the incident light thus enabling our quantum well to act as a polarization detector. The respective transition probabilities are summarized in Table I.[23] The TE polarized light, with an electrical field vector oscillating in the plane of the quantum well, can excite both the $e_0-\mathrm{lh}_0$ and $e_0-\mathrm{hh}_0$ transitions with the heavy hole transition being three times stronger than the light hole transition. With light polarized along the growth direction of our sample (TM polarization), only $e_0-\mathrm{lh}_0$ transitions can be excited.

Figure 2 shows a photocurrent measurement for the two orthogonal linear polarizations TE and TM when illuminating the sample in a waveguide configuration (see inset in Fig. 2). The sample used in the waveguide geometry was similar to the one depicted in Fig. 1. In the waveguide structure thick layers with high aluminum content defined the cladding of an optical waveguide by modulation of the refractive index. The optoelectronic properties of the quantum well in the waveguide structure and that depicted in Fig. 1 are, however, identical. The excitation light from a monochromator was coupled into the waveguide at the cleaved edge of the sample and guided in the plane of the quantum well over a distance of 500 μm.[24] This method enables easy alignment of the linear polarization to be either along the growth direction or in the quantum well plane, respectively. As can be seen in Fig. 2, TM-polarized light couples to the $e_0-\mathrm{lh}_0$ transition only, whereas for TE polarization, both the $e_0-\mathrm{lh}_0$ and $e_0-\mathrm{hh}_0$ transitions contribute to the photocurrent spectrum. This polarization sensitivity can be exploited to determine the amount of longitudinal electric field in the focal region of a focused light beam. To accomplish this, the focusing beam has to be incident onto the sample from the growth direction. For this geometry the longitudinal component corresponds to TM polarization, whereas the transverse component corresponds to TE polarization. When focusing a beam of an unknown polarization, the amount of longitudinal electric field in the focal region can be extracted from the spectrum by comparing the absorption peaks against a reference spectrum obtained for pure TE polarization. In our experiment we use radially and azimuthally polarized beams. The focal region of a focused radially polarized field comprises of a mixture of TE and TM components. A focused azimuthally polarized beam is everywhere transverse (pure TE polarization) and therefore presents a good choice of a reference.

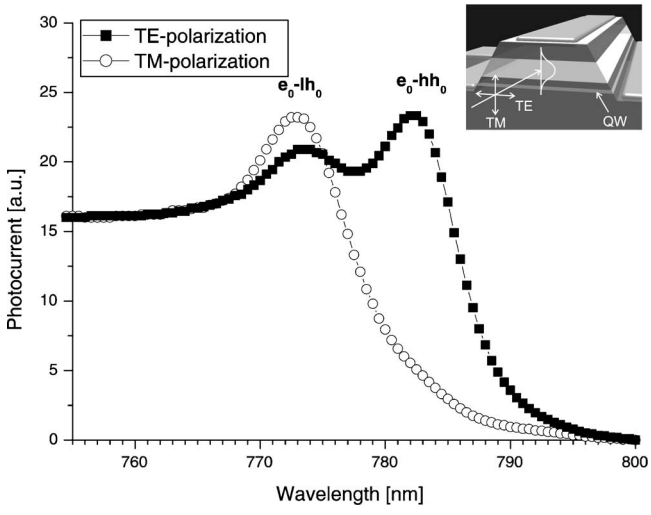

FIG. 2. Polarization resolved photocurrent measurement of a sample with a quantum well embedded into an optical waveguide structure. The quantum well in this structure is identical to that of the sample used for normal incidence illumination. With light polarized along the growth direction (TM mode) only $e_0-\mathrm{lh}_0$ transitions can be excited. In contrast, both the $e_0-\mathrm{lh}_0$ and $e_0-\mathrm{hh}_0$ transitions contribute to the photocurrent spectrum if the excitation light is polarized parallel to the quantum well plane (TE mode). Inset: Illumination of the sample from the in-plane geometry.

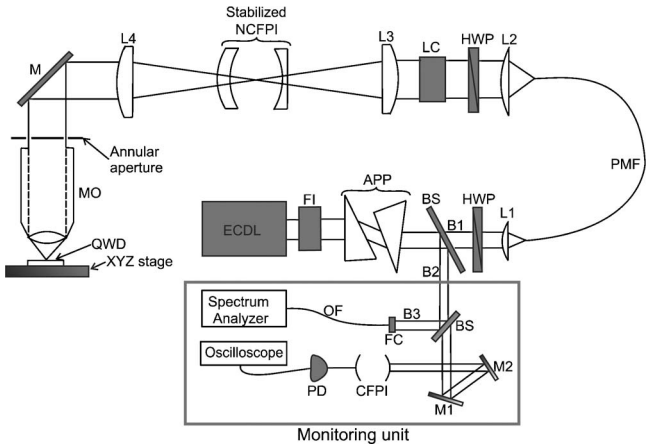

FIG. 3. The experimental setup to generate radially and azimuthally polarized beams. A microscope objective (MO) (NA=0.9) focuses the beam onto the quantum well detector (QWD).

III. EXPERIMENTAL SETUP

The experimental setup used to generate radially and azimuthally polarized beams at wavelengths between 762 and 787 nm is depicted in Fig. 3. An external cavity diode laser (ECDL) in Littman configuration is used as a light source. After beam shaping using an anamorphic prism pair (APP), the laser beam is focused into a single mode polarization maintaining fiber (PMF) for spatial mode filtering. The monitoring unit measures the laser wavelength and also gives an indication of the stability of the laser over the tuned wavelength range. The output beam from the fiber is collimated to a beam diameter of $\approx$3.75 mm. The key element of our setup is the liquid crystal (LC) device[25] which is used to modify the polarization properties of our laser beam. By rotating the input polarization locally, the liquid crystal device transforms a linearly polarized beam into a rotationally symmetrical polarized output. The half-wave plate (HWP) in front of the liquid crystal device is used to set the plane of linear polarization in such a way that the transmitted beam is either radially or azimuthally polarized. The output from the liquid crystal is coupled into a stabilized nonconfocal Fabry-Perot interferometer (NCFPI) which is used to suppress

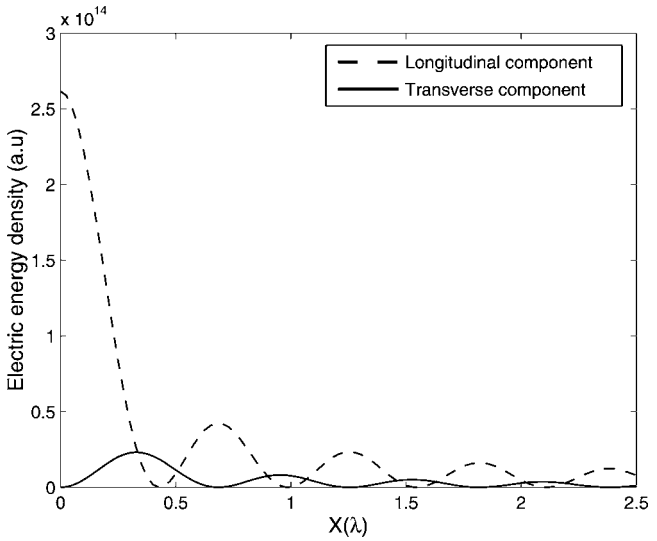

FIG. 4. The electric energy density of the longitudinal and transverse components in air. E_z is the longitudinal component and E_x represents the transverse component.

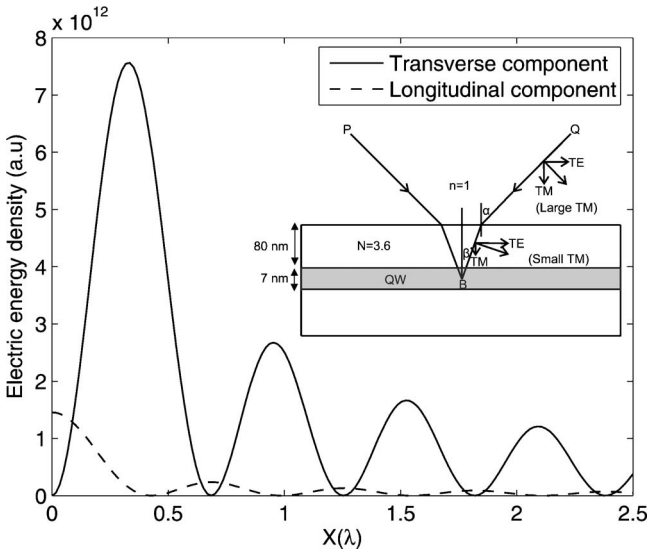

FIG. 5. The electric energy density of the longitudinal and transverse field components inside the quantum well after refraction at the interface. Inset: *P* and *Q* are the peripheral rays from the high NA microscope objective. Point *B* indicates the position of the focal spot inside the quantum well. α and β are the angles of incidence and refraction, respectively.

higher order modes due to the Gouy phase shift.[26] A collimating lens (L4) is chosen so that the doughnut mode from the NCFPI has a beam waist equal to the radius of the entrance aperture of the microscope objective (MO). A set of four mirrors (*M*) for polarization insensitive deflection guides the beam onto the microscope objective. The entrance pupil of the microscope objective is 3.6 mm in diameter, and an annular aperture of 3.3 mm in diameter is used to block the center part of the beam. This enhances the longitudinal electric field at the focus of the high NA microscope objective. The microscope objective focuses the beam onto the quantum well structure, which is mounted on a three-dimensional (3D) piezostage. After moving the quantum well into the focal region, wavelength dependent photocurrent spectra are measured.

IV. SIMULATION

Simulation results based on vector diffraction theory[27] show that the focused radially polarized beam has an approximately 80% longitudinal component in air. Figure 4 gives an idea about the relative strengths of the longitudinal and transverse components in air. If the focusing beam is propagating through an interface, refraction occurs at the boundary. The maximum angle of incidence α in air is given by $\sin^{-1}(NA)$, i.e., $\alpha \approx 64°$. This reduces to $\beta = 14.5°$ in GaAs ($n_{\mathrm{GaAs}} \approx 3.6$) after refraction at the air-GaAs interface. As a result, the superposing light rays at the focus have a strongly reduced longitudinal component and a dominating transverse component compared to the focus in air. Figure 5 shows the result of a theoretical calculation and it reveals the relative strengths of the two components inside the quantum well structure. In this case, the focal spot comprises only of about 9% of longitudinal component.

For a given input power the absorption in the quantum well differs for radial and azimuthal polarization due to the polarization dependence of the Fresnel coefficients. The simulation yields 2.35 as the power ratio between the two polarizations.

V. EXPERIMENTS AND DISCUSSION

Photocurrent measurements, which are a direct measure of absorption, were performed for both radially and azimuthally polarized beams by tuning the laser wavelength between 762 and 787 nm. The photocurrent spectrum for an azimuthally polarized input field (pure TE) which was used as a reference is depicted in Fig. 6(a). Both the $e_0-\mathrm{lh}_0$ and $e_0-\mathrm{hh}_0$ transitions are clearly resolved as individual peaks in the photocurrent spectrum.

For fitting the experimental data, we use a semiempirical approach,

$$I_{\mathrm{ph}(azi.)} \propto \underbrace{\frac{3}{12} I^{\mathrm{hh}}(\lambda) + \frac{1}{12} I^{\mathrm{lh}}(\lambda)}_{\text{TE-absorption}}. \tag{1}$$

The contributions to the photocurrent due to the light hole absorption $[I^{\mathrm{lh}}(\lambda)]$ and heavy hole absorption $[I^{\mathrm{hh}}(\lambda)]$ are weighted with the coefficients given by the polarization dependent transition probabilities for pure TE polarized excitation light (Table I). The individual contributions $[I^{\mathrm{lh}}(\lambda)$ and $I^{\mathrm{hh}}(\lambda)]$ are parameterized functions chosen empirically to model the shape of the corresponding absorption contribution. Each of them consists of two-halves of Gaussian functions with the maximum corresponding to the transition energy of the excitonic ground state and a step function to model the exciton excited states and the [two-dimensional (2D)] continuum (Fig. 7). The fitting procedure results in a set of parameters (Table II) which fully describe the light and heavy hole contributions separately as presented also in Fig. 6(a).

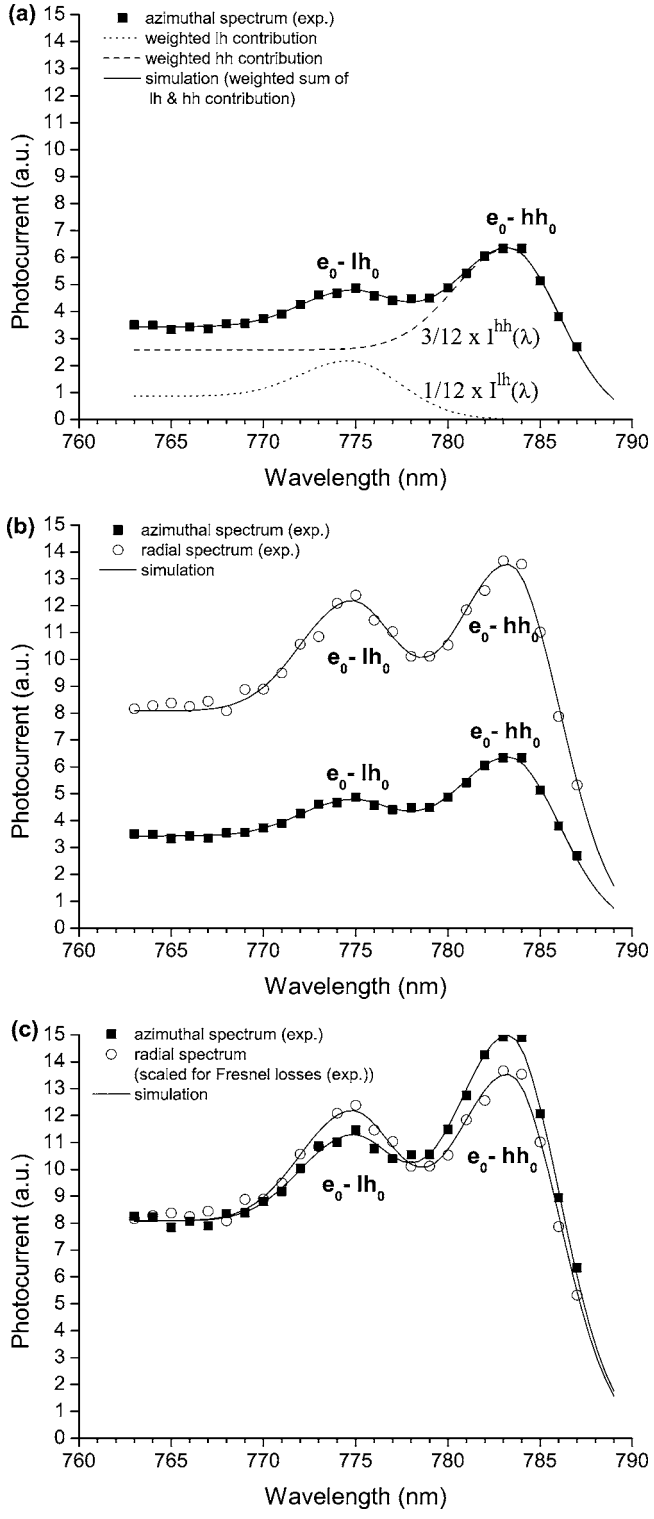

FIG. 6. (a) Photocurrent spectrum for azimuthally polarized beam. $e_0-\mathrm{lh}_0$ light hole absorption peak and $e_0-\mathrm{hh}_0$ heavy hole absorption peak. Also included are the simulated contributions, $(3/12)I^{\mathrm{hh}}(\lambda)$ and $(1/12)I^{\mathrm{lh}}(\lambda)$ due to light and heavy hole absorptions, respectively. (b) Photocurrent spectra (data points) for azimuthal and radial polarization together with the simulated spectra (lines). (c) Comparison between the photocurrent spectra for radially and azimuthally polarized beams normalized at the plateau (at ~765 nm).

These two functions are used to extract the amount of the longitudinal component for the radially polarized beam. In Fig. 6(b), two spectra recorded with the same beam power for azimuthally and radially polarized excitation light are

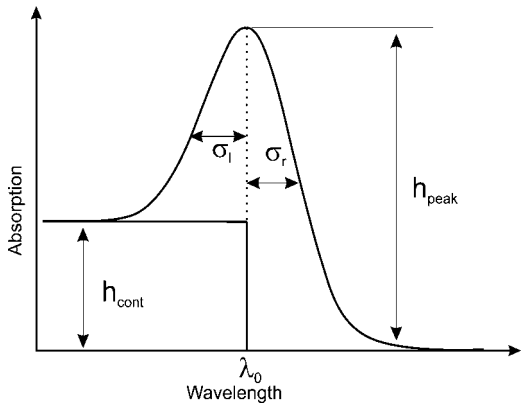

FIG. 7. Illustration of the parameters used for the fit functions for the light and heavy hole absorption contributions.

depicted. In the latter case the photocurrent is higher due to the lower Fresnel losses for the radially polarized beam. With a longitudinal component present in the focal region, the shape of the radial spectrum differs from that of the azimuthal spectrum as can be seen in Fig. 6(c), where the two spectra are normalized to the excitonic continuum. The longitudinal field component present in the focused radially polarized field clearly reduces the absorption strength of the heavy holes, whereas that of the light holes is enhanced.

The amount of the longitudinal component x present in the spectrum for radial polarization was finally extracted by mixing the light and heavy hole contributions with the respective weights. For our radial spectrum with an unknown amount x of the TM component and $(1-x)$ of the TE component in the total electric energy density, the fit function given in Eq. (2) was used to model the experimental data. It consists of two contributions accounting for the absorption of the TM- and TE-polarized components, multiplied by the relative strength of the corresponding component x and $(1-x)$, respectively.

Finally, the sum is scaled by a factor τ to match the experimental data. For the individual light and heavy hole contributions $[I^{\mathrm{lh}}(\lambda)$ and $I^{\mathrm{hh}}(\lambda)]$, in Eq. (2) the functions found for the azimuthal spectrum were used, thus restricting the fitting procedure to the variation of only the two parameters x and τ.

$$I_{\mathrm{ph(rad.)}} \propto \underbrace{\tau\left\{x\left[\frac{4}{12}I^{\mathrm{lh}}(\lambda)\right]\right\}}_{\text{TM-absorption}} + \underbrace{\tau\left\{(1-x)\left[\frac{3}{12}I^{\mathrm{hh}}(\lambda)+\frac{1}{12}I^{\mathrm{lh}}(\lambda)\right]\right\}}_{\text{TE-absorption}}. \tag{2}$$

The resulting fit for the spectrum with radially polarized input field using this method is plotted in Figs. 6(b) and 6(c) as the simulated spectrum. It fits the measured data points very well. The fraction of the longitudinal component x was found to be 9.8% in our experiment, whereas vector diffraction theory discussed above predicts a value of 9%. The scaling factor τ corresponds to the ratio of the transmitted power of the radially polarized beam to the azimuthally polarized

TABLE II. Coefficients for the light and heavy hole absorption function resulting from the fit procedure for azimuthal polarization.

	σ_l (nm)	σ_r (nm)	λ_0 (nm)	h_{cont} (a. u.)	h_{peak} (a. u.)
hh	4.2	3.9	783.3	0.86	2.1
lh	3.8	3.9	774.6	0.86	2.2

beam. A value of 2.35 was obtained for τ which agrees to the digit with the theoretical value.

VI. CONCLUSION

We have shown that quantum well nanostructures are well suited for measuring the amount of longitudinal polarization present at the focal spot of a highly focused laser beam. Using the quantum well structure we were able to determine the overall fraction of the longitudinal electric field component by taking into account the refraction at the sample surface. The longitudinal component is reduced from 80% to 9% by refraction at the sample surface. To avoid refraction and to enhance the effect, a solid immersion lens[28] (SIL) of the same refractive index as the semiconductor structure should ideally be used. In this case, the proportions of the transverse and longitudinal components in air are preserved when the focusing incident wavefront has the same curvature as the SIL. A simulation for that case is shown in Fig. 8. The amount of longitudinal component is then only limited by the (numerical aperture) NA of the microscope objective used.[28,29]

To investigate the spot size and the polarization properties, we propose also "zero-dimensional" nanostructures [e.g., InAs self-assembled quantum dots (SAD's] as an appealing tool.[30] These structures are much smaller than the wavelength of light and therefore allow for a high spatial resolution. To distinguish between longitudinal and transverse fields, the strong heavy and light hole splitting in SAD's (Refs. 22) could be used. However, to implement this aspect in the present experiment the spectral range has to be shifted to the near IR region of about 1.2 μm.

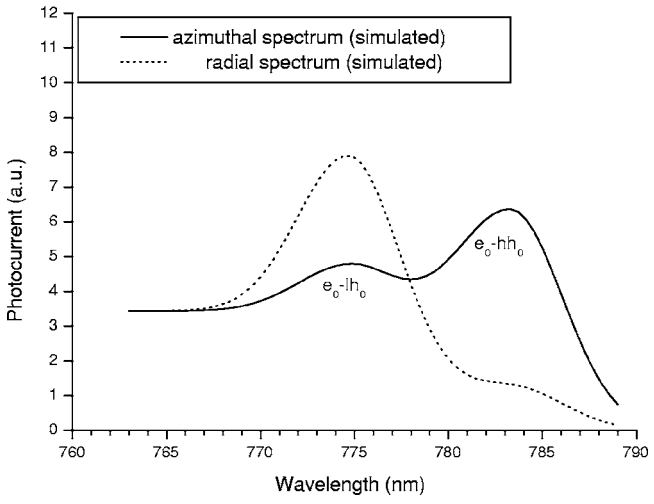

FIG. 8. Simulated spectra for radially and azimuthally polarized light when using a SIL of the same material as that of the sample. The heavy hole peak is suppressed indicating a high proportion of the longitudinal component.

ACKNOWLEDGMENTS

One of the authors (G.K.R.) is grateful to *Deutsche Akademische Austauschdienst* (DAAD) for the support during this work.

[1] B. Richards and E. Wolf, Proc. R. Soc. London, Ser. A **253**, 358 (1959).
[2] R. Dorn, S. Quabis, and G. Leuchs, J. Mod. Opt. **50**, 1917 (2003).
[3] L. Novotny, E. J. Sanchez, and X. S. Xie, Ultramicroscopy **71**, 21 (1998).
[4] V. G. Niziev and A. V. Nesterov, J. Phys. D **32**, 1455 (1999).
[5] R. D. Romea and W. D. Kimura, Phys. Rev. D **42**, 1807 (1990).
[6] R. Dorn, S. Quabis, and G. Leuchs, Phys. Rev. Lett. **91**, 233901 (2003).
[7] In this paper intensity refers to the electric energy density, which is the part of the electric field energy that couples to standard photodetectors and photosensitive materials.
[8] G. P. Karman, A. Van Duijl, M. W. Beijersbergen, and J. P. Woerdman, Appl. Opt. **36**, 8091 (1997).
[9] A. H. Firester, M. E. Heller, and P. Sheng, Appl. Opt. **16**, 1971 (1977).
[10] S. K. Rhodes, K. A. Nugent, and A. Roberts, J. Opt. Soc. Am. A **19**, 1689 (2002).
[11] A. Nesci, R. Dändliker, and H.-P. Herzig, Opt. Lett. **26**, 208 (2001).
[12] E. Descrovi, L. Vaccaro, L. Aeschimann, W. Nakagawa, U. Staufer, and H.-P. Herzig, J. Opt. Soc. Am. A **22**, 1432 (2005).
[13] K. Bahlmann and S. W. Hell, Appl. Phys. Lett. **77**, 612 (2000).
[14] A. Bouhelier, M. R. Beversluis, and L. Novotny, Appl. Phys. Lett. **82**, 4596 (2003).
[15] C. Debus, M. A. Lieb, A. Drechsler, and A. J. Meixner, J. Microsc. **210**, 203 (2003).
[16] N. Hayazawa, Y. Saito, and S. Kawata, Appl. Phys. Lett. **85**, 6239 (2004).
[17] T. Wilson, R. Juskaitis, and P. Higdon, Opt. Commun. **141**, 298 (1997).
[18] B. Sick, B. Hecht, and L. Novotny, Phys. Rev. Lett. **85**, 4482 (2000).
[19] L. Novotny, M. R. Beversluis, K. S. Youngworth, and T. G. Brown, Phys. Rev. Lett. **86**, 5251 (2001).
[20] J. S. Weiner, D. A. B. Miller, D. S. Chemla, T. C. Damen, C. A. Burrus, T. H. Wood, A. C. Gossard, and W. Wiegmann, Appl. Phys. Lett. **47**, 1148 (1985).
[21] J. S. Weiner, D. S. Chemla, D. A. B. Miller, H. A. Haus, A. C. Gossard, W. Wiegmann, and C. A. Burrus, Appl. Phys. Lett. **47**, 664 (1985).
[22] O. Wolst, M. Kahl, M. Schardt, S. Malzer, and G. H. Dohler, Physica E (Amsterdam) **17**, 554 (2003).
[23] G. Bastard, *Wave Mechanics Applied to Semiconductor Heterostructures* (Les Editions de Physique, Les Ulis, 1988), p. 247.
[24] By positioning the quantum well inside the cladding layers of the optical waveguide, one can gain precise control of the overlap between the well and the optical modes, thus enabling adjustment for only weak absorption per unit length.
[25] M. Stalder and M. Schadt, Opt. Lett. **21**, 1948 (1996).
[26] S. Quabis, R. Dorn, and G. Leuchs, Appl. Phys. B: Lasers Opt. **81**, 597 (2005).
[27] A. S. van de Nes, L. Billy, S. F. Pereira, and J. J. M. Braat, Opt. Express **12**, 1281 (2004).
[28] S. M. Mansfield and G. S. Kino, Appl. Phys. Lett. **57**, 2615 (1990).
[29] L. E. Helseth, Opt. Commun. **191**, 161 (2001).
[30] B. B. Goldberg, S. B. Ippolito, L. Novotny, Z. Liu, and M. S. Unlu, IEEE J. Sel. Top. Quantum Electron. **8**, 1051 (2002).